ACS NANO
www.acsnano.org
ARTICLE

Li Electrochemical Tuning of Metal Oxide for Highly Selective CO_2 Reduction

Kun Jiang,[†] Han Wang,[‡] Wen-Bin Cai,[‡] and Haotian Wang*[,†]

[†]Rowland Institute, Harvard University, Cambridge, Massachusetts 02142, United States

[‡]Shanghai Key Laboratory of Molecular Catalysis and Innovative Materials, Collaborative Innovation Center of Chemistry for Energy Materials, Department of Chemistry, Fudan University, Shanghai 200433, China

Supporting Information

ABSTRACT: **Engineering active grain boundaries (GBs) in oxide-derived (OD) electrocatalysts is critical to improve the selectivity in CO_2 reduction reaction (CO_2RR), which is becoming an increasingly important pathway for renewable energy storage and usage. Different from traditional *in situ* electrochemical reduction under CO_2RR conditions, where some metal oxides are converted into active metallic phases but with decreased GB densities, here we introduce the Li electrochemical tuning (LiET) method to controllably reduce the oxide precursors into interconnected ultrasmall metal nanoparticles with enriched GBs. By using ZnO as a case study, we demonstrate that the LiET-Zn with freshly exposed GBs exhibits a CO_2-to-CO partial current of ~23 mA cm^{-2} at an overpotential of −948 mV, representing a 5-fold improvement from the OD-Zn with GBs eliminated during the *in situ* electro-reduction process. A maximal CO Faradaic efficiency of ~91.1% is obtained by LiET-Zn on glassy carbon substrate. The CO_2-to-CO mechanism and interfacial chemistry are further probed at the molecular level by advanced *in situ* spectroelectrochemical technique, where the reaction intermediate of carboxyl species adsorbed on LiET-Zn surface is revealed.**

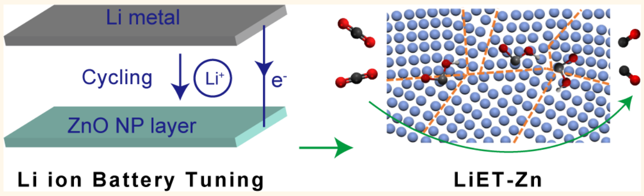

KEYWORDS: *lithium electrochemical tuning, carbon dioxide reduction, zinc catalyst, grain boundaries, in situ surface-enhanced infrared absorption spectroscopy*

In facing global energy and environmental concerns, developing alternative energy technologies to reduce carbon emission from fossil fuels is of central interest over the years.[1] As the price of renewable energy continuous to decrease, efficiently converting clean electricity into chemicals or fuels is not only environmentally benign but also is becoming an economical option.[2] One of the most attractive pathways is to electrochemically drive room-temperature carbon dioxide (CO_2) reduction into value-added chemicals and/or fuel molecules, and potentially close the anthropogenic carbon circle.[3−7] However, since water is the most widely used reaction media and proton donator,[8] selective CO_2 reduction reaction (CO_2RR) becomes a great challenge due to the strong competition with the hydrogen evolution reaction (HER), especially under significant overpotentials.[9−12] This requires catalysts to have specific electronic structures, which could properly bind different reaction intermediates and thus facilitate CO_2RR and suppress HER.[13−16] As a representative example, noble metals such as Au[12,17−19] or Ag[20−22] can covert CO_2 to carbon monoxide (CO) at relatively high Faradaic efficiencies (FEs), while Pt with only one d-orbital electron less generates H_2 exclusively under CO_2RR conditions.[23,24] Other earth-abundant metals, including Cu,[9,25−31] Co,[10,32] Sn,[33−36] Zn,[37−40] and so on, have also been screened and demonstrated to be selective to CO, formic acid, methane (CH_4), or even C_{2+} products. However, in those bulk catalytic metals, there is still a significant portion of current injected into H_2. How to further upgrade their CO_2RR performances through proper morphological and/or electronic structure tuning is now becoming increasingly important.

Among the different electronic structure tuning methods, such as surface ligand coating,[41,42] metal alloying,[43−45] metal−organic frameworks,[11,46] molecular metal−organics,[47,48] and so on, the oxide-derived (OD) metal catalysts have attracted particular interests due to their significant improvements in CO_2RR FEs.[10,18,25−28,32−35,49] Many types of metal oxides or sulfides, according to the Pourbaix diagram, are electrochemically reduced into the active metallic phases under CO_2RR conditions usually with significantly negative potentials. Different from the thermal annealing process under H_2, the electrochemical reduction is usually finished within a short time, suggesting a nonequilibrium oxide to metal phase transition and thus generating a number of grain boundaries (GBs). Those GBs are generally rich in lattice defects, dislocations, distortions, or local strains with unique electronic

Received: May 2, 2017
Accepted: May 30, 2017
Published: May 30, 2017

DOI: 10.1021/acsnano.7b03029
ACS Nano XXXX, XXX, XXX−XXX

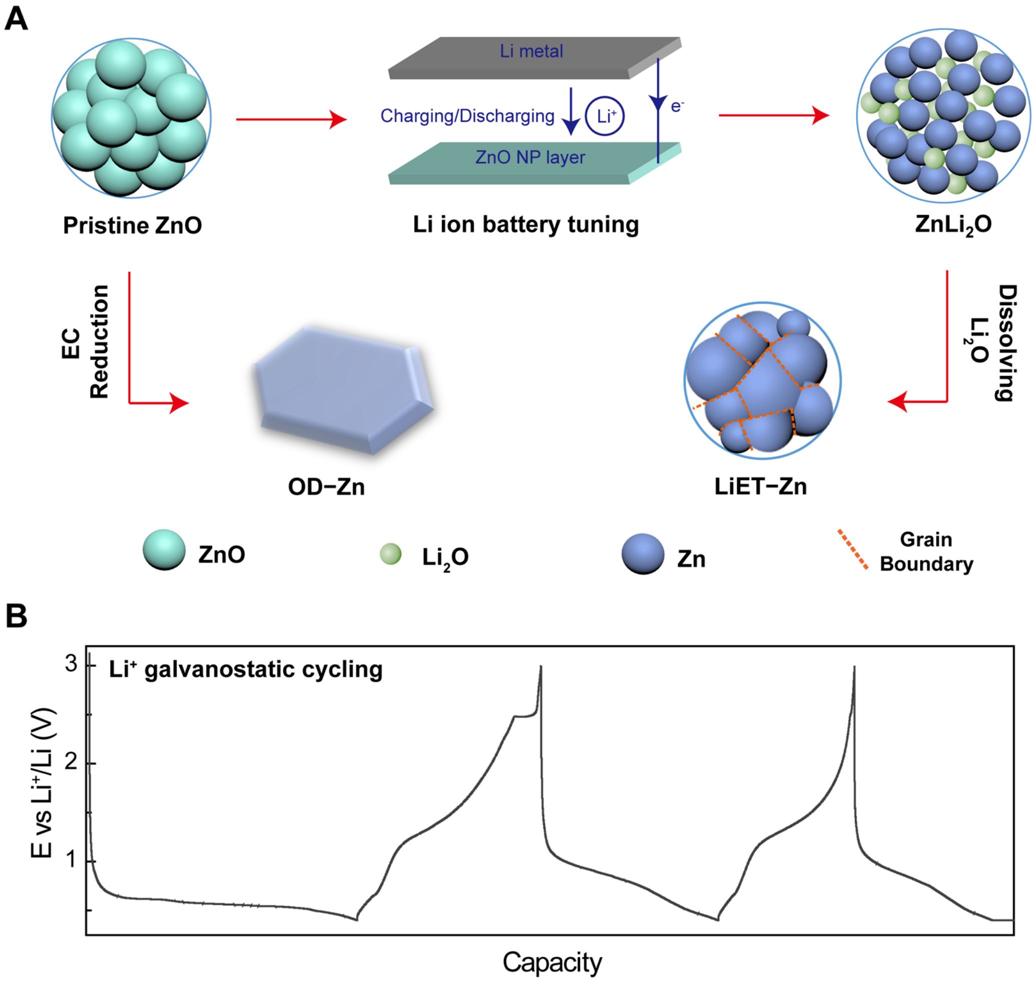

Figure 1. Schematic of ZnO structure evolution by different reduction methods and the voltage profile of Li electrochemical tuning method. (A) ZnO NPs gradually evolve into either interconnected Zn NPs with enriched GBs by Li^+ charging/discharging cycles or larger Zn single-crystalline NPs by traditional *in situ* electrochemical reduction under CO_2RR conditions. (B) Galvanostatic battery cycling curves representing Li^+ charging/discharging profile.

structures, which are critical for significantly improved CO_2RR selectivity.[18,25−28,33−35,49] However, depending on the material properties of different metal oxides as well as the electrochemical reduction conditions, the GB densities in OD metals may vary dramatically. For example, some metal oxides, such as ZnO or Bi_2O_3, with relatively low electrical conductivities may slowly get reduced from the contact with substrate. During this process, small oxide nanoparticles (NPs) could get merged together into bulk crystalline,[50] decreasing the GB densities and thus the active metal sites (Figure 1A). Therefore, how to maintain or even increase as many as possible GBs during the reduction process remains as a challenge for boosting the catalytic CO_2RR performance.

Inspired from studies in transition-metal oxide Li-ion batteries (LIBs), here we introduce the Li electrochemical tuning method,[15,51] to controllably reduce the metal oxide precursor into metallic phase while generating a number of GBs. It has been observed in LIB studies that during the battery charging process, with the insertion of Li ions, metal oxides are reduced into ultrasmall metal NPs embedded in a Li_2O matrix.[52] With Li_2O gradually dissolved in nonaqueous solutions, GBs would be created between those tiny metal NPs (Figure 1A).[53] Here we use ZnO as a representing material to study the efficacy of Li electrochemical tuning method in improving CO_2RR selectivity. Limited cycles of Li^+ insertion and extraction (Figure 1B) from ZnO lattice are carried out to generate the interconnected Zn NPs ($ZnO + 2Li^+ + 2e^- \rightarrow Zn + Li_2O$ with freshly exposed GBs (LiET-Zn). As a result, the LiET-Zn delivers a CO partial current density of ~23 mA cm^{-2} at an overpotential of −948 mV in aqueous electrolyte, representing a nearly 5-fold improvement compared to the OD Zn metal catalyst (OD-Zn) from traditional electrochemical reduction, where GBs are significantly reduced. By using a mirror-polished glassy carbon substrate to minimize the HER contribution from the current collector, the LiET-Zn presents a maximum CO FE of ~91.1%. In addition, using this CO selective LiET-Zn as a model catalyst, we probed the CO_2-to-CO reaction pathway at the molecular level by *in situ* attenuated total reflection surface-enhanced IR absorption spectroscopy (ATR-SEIRAS), revealing the surface bonded carboxyl species as an active intermediate in CO evolution.

RESULTS AND DISCUSSION

ZnO NPs were first uniformly grown on carbon fiber paper (CFP) substrates by a previously developed dip-coating and thermal annealing method (Figure 2A and Methods). Those NPs with small sizes of tens of nanometers are interconnected with each other to form a relatively larger mother particle as

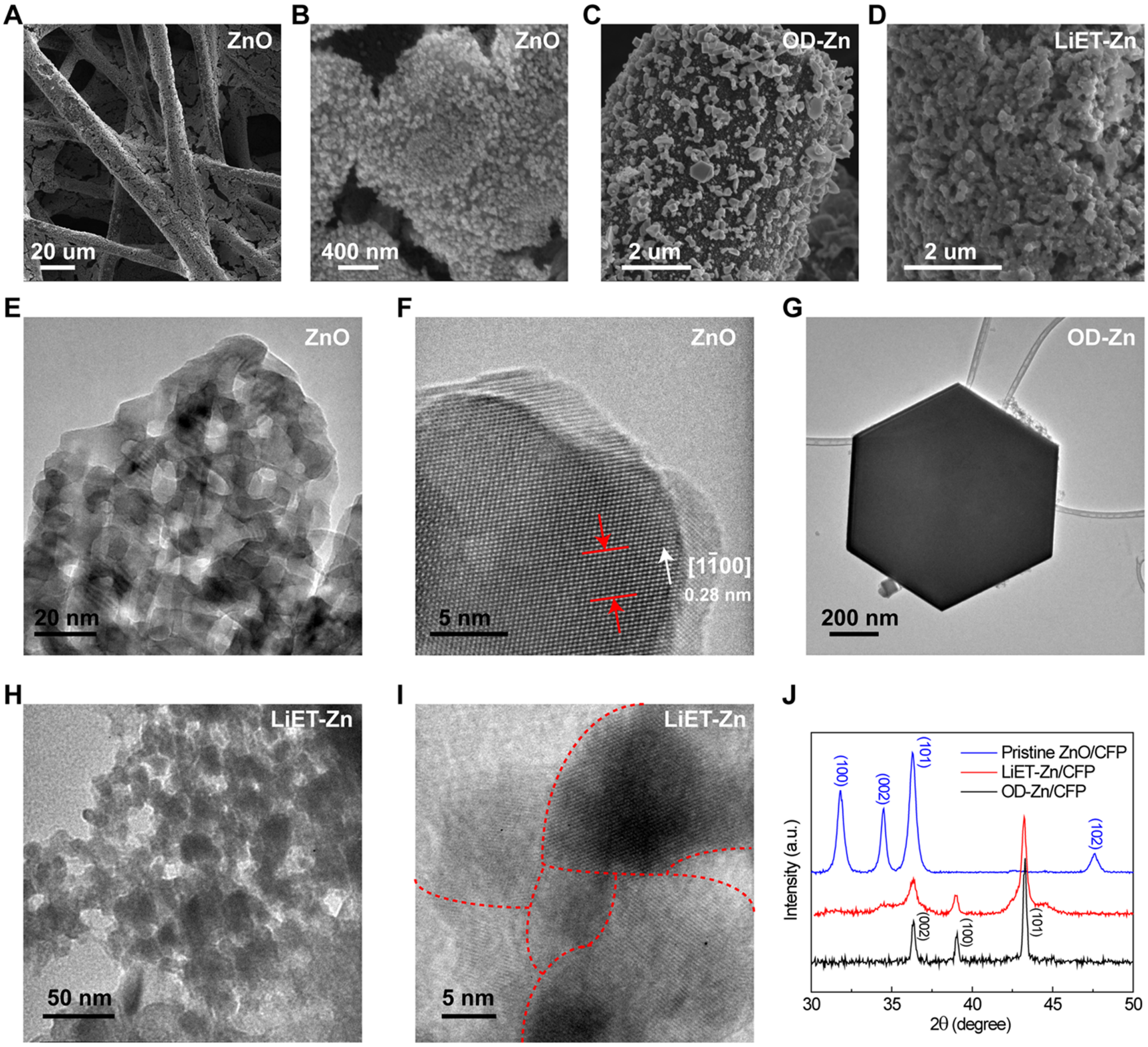

Figure 2. Characterizations of zinc catalysts on CFP. (A, B) SEM images of pristine ZnO NPs on CFP. (C) SEM image of OD-Zn NPs on CFP. Smooth surfaces and well-defined shapes of the NPs are observed. (D) SEM image of LiET-Zn NPs on CFP. Similar to the pristine ZnO, the LiET-Zn NPs remain small in size and interconnected. (E, F) TEM images of pristine ZnO. The average lattice spacing of $(1\bar{1}00)$ was measured to be 0.28 nm by integrating the image pixels along a few atomic layers as indicated by the red arrows (Figure S2), consistent with ZnO lattice parameters. (G) TEM image of an OD-Zn hexagonal nanoplate related to the Zn metal hexagonal close-packed crystal structure, suggesting its single-crystalline nature. (H, I) TEM images of LiET-Zn. Different from OD-Zn, LiET-Zn particles with small sizes are interconnected with each other, presenting a number of fresh GBs. (J) XRD of pristine ZnO, LiET-Zn, and OD-Zn. The XRD pattern of ZnO is a typical wurtzite structure (PDF no. 36-1451). Both LiET-Zn and OD-Zn show a Zn metal XRD pattern (PDF no. 04-0831). LiET-Zn shows a much broader XRD peak feature than OD-Zn, indicating the smaller sizes of the metallic NPs.

shown in scanning electron microscopy (SEM) images (Figure 2B). More detailed characterizations have been performed using transmission electron microscopy (TEM). The larger particle shows a mesoporous structure (Figure 2E),[39] where those interconnected small particles (~20 nm) present a single crystalline nature but with varied orientations (Figure 2F). However, this morphology is completely changed after the electrochemical reduction of ZnO to Zn under CO_2RR conditions (see Methods). The OD-Zn NPs show an increased particle size of a few hundred nanometers and, more importantly, present smooth surfaces (Figure 2C) and well-defined particle shapes such as a hexagonal plate in Figure 2G, indicating their single-crystalline nature. Since ZnO has a wide bandgap and thus low electrical conductivity,[54] the electrochemical reduction process may gradually propagate from the contact with the support to the very top of the mother particles, during which those interconnected ZnO NPs may easily merge together to become a bigger single-crystalline Zn NP. This as a result significantly reduces the GB densities in the OD-Zn catalyst and thus would decrease the CO_2RR activity and selectivity. To generate as many as possible GBs, we constructed a ZnO-LIB configuration to electrochemically insert Li ions into ZnO, during which the ZnO NP is converted into ultrasmall Zn NPs embedded in the Li_2O matrix.[15] A few Li^+ insertion and extraction cycles were followed to further reduce the particle sizes and create more

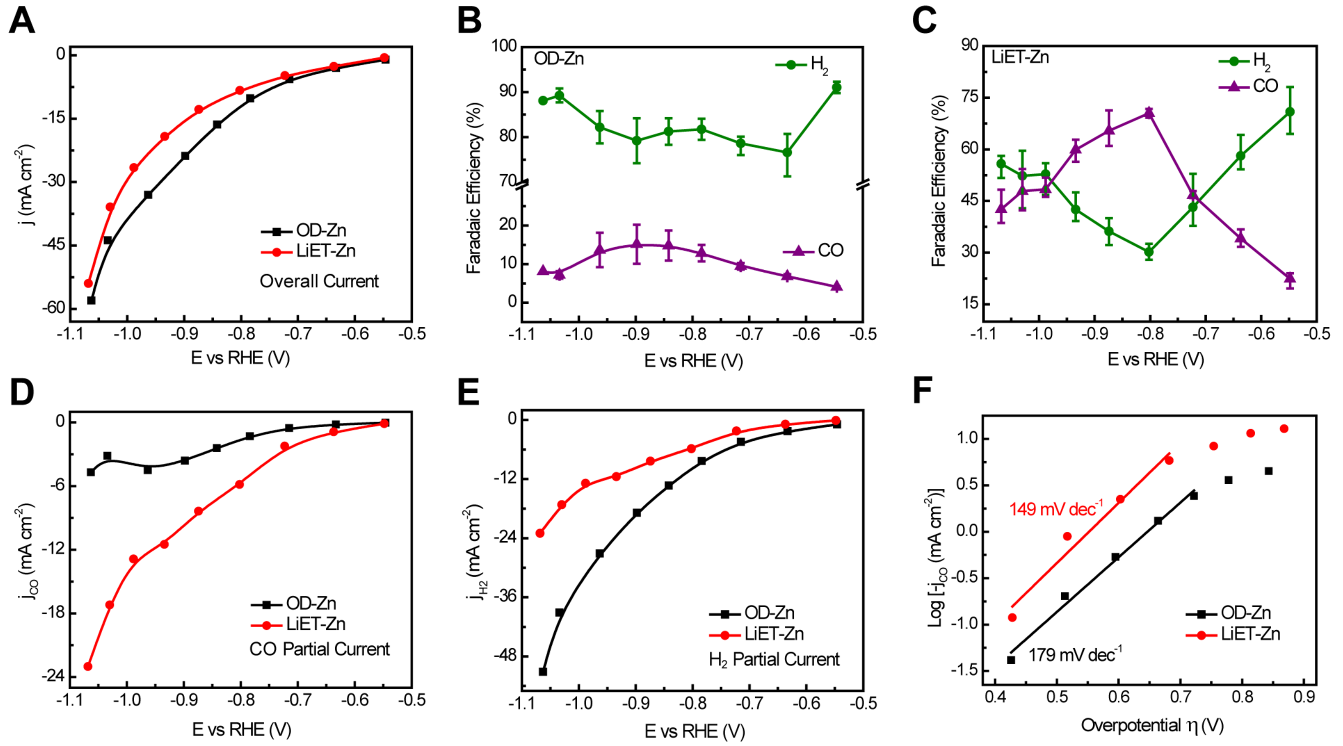

Figure 3. Electrocatalytic CO_2RR performances on OD-Zn and LiET-Zn on CFP substrate. (A) Steady-state current densities at each potential during CO_2RR electrolysis in CO_2-saturated 0.1 M $KHCO_3$. (B, C) FEs of H_2 and CO at different applied potentials for OD-Zn and LiET-Zn. The maximal CO FE of LiET-Zn on CFP is 71% at −0.8 V *vs* RHE, which is ∼5.5 times of 12.9% for OD-Zn. (D, E) Comparisons of H_2 and CO partial current densities between LiET-Zn and OD-Zn. Under an overpotential of −948 mV, LiET-Zn delivers a CO partial current density 5 times of that by OD-Zn, while suppresses HER with a H_2 partial current nearly half of OD-Zn. (F) The Tafel slope of CO evolution in LiET-Zn is slightly improved from that of OD-Zn.

GBs and defects.[53] The cycling process was stopped at the charging status of 0.4 V *vs* Li^+/Li, which is negative enough to initially reduce ZnO into metals, as suggested by the X-ray diffraction (XRD, Figure 2J) and X-ray photoelectron spectroscopy (XPS, Figure S1), before the CO_2RR catalysis. This as-prepared metallic phase would help to prevent the particle aggregation during the traditional electrochemical reduction process in CO_2RR and thus preserve active GBs. Different from the single-crystalline OD-Zn NPs, the LiET-Zn NPs in Figure 2H,I present ultrasmall grains of ∼10−20 nm interconnected with each other, providing a number of GBs to boost the CO_2RR performance. This is also confirmed by XRD where the LiET-Zn shows broader peaks than those of OD-Zn, representing the significantly reduced particle sizes (Figure 2J).

The electrocatalytic CO_2RR performances over OD-Zn and LiET-Zn catalysts grown on CFPs were evaluated in a customized H-cell with CO_2-saturated 0.1 M $KHCO_3$ as the electrolyte (see Methods). With the same Zn loading (3 mg cm^{-2}), both catalysts showed similar geometric current densities (Figures 3A and S3). Based on the Pourbaix diagram, ZnO can be reduced to Zn metal under −0.5 V *vs* RHE (Figure S4). The prereduction process has been monitored by Raman spectroscopy under different potentials, with oxide signals gradually decreased at −0.63 V *vs* RHE and readily disappeared under more negative potentials (Figure S5).[55] Only H_2 and CO were detected as the major electrocatalytic products during CO_2RR, consistent with previous literatures of Zn catalysts.[23,37−40] As shown in Figure 3B, H_2 is the predominant product by OD-Zn over the whole potential range, with a CO FE <20%, similar to the bulk Zn metal materials.[38,40] The CO_2RR performance was significantly improved after the Li electrochemical tuning process with freshly exposed GBs in LiET-Zn, with an optimized CO selectivity obtained after three cycles of lithiation/delithiation processes (Figure S6). A volcano-like curve of CO FE was observed in Figure 3C: The CO FE gradually increases from 22% at −0.55 V *vs* RHE to a peak of 71% (5.5 times of OD-Zn) at −0.8 V *vs* RHE and then decreases to 43% at larger overpotentials, possibly due to the significant HER contributions from the CFP support (Figure S7). To better illustrate the differences of activity and selectivity between LiET-Zn and OD-Zn, the partial current densities of CO and H_2 were plotted accordingly in Figure 3D,E. LiET-Zn exhibited a j_{CO} of ∼23 mA cm^{-2} at an overpotential of −948 mV, which is ∼5 times of the CO evolution current by OD-Zn, while only catalyzed half of the HER current of OD-Zn. This trend clearly demonstrates the dramatically improved CO selectivity of LiET-Zn due to those GBs created by the Li electrochemical tuning method. In addition, the CO_2-to-CO Tafel slope of LiET-Zn is 149 mV decade^{-1}, smaller than the OD-Zn of 179 mV decade^{-1}, suggesting the slightly improved kinetics in CO evolution (Figure 3F).

To avoid a significant HER contribution from CFP substrate especially under large overpotentials, we instead use a mirror polished glassy carbon electrode with minimized HER side reaction from the support and study the intrinsic CO_2RR selectivity of LiET-Zn (Figure S7). We further extended this Li electrochemical tuning method to commercially available ZnO nanopowders which can be easily and uniformly drop-casted onto glassy carbon electrode (see Methods). A remarkable CO FE up to 91.1% was achieved at −1.17 V *vs* RHE with largely

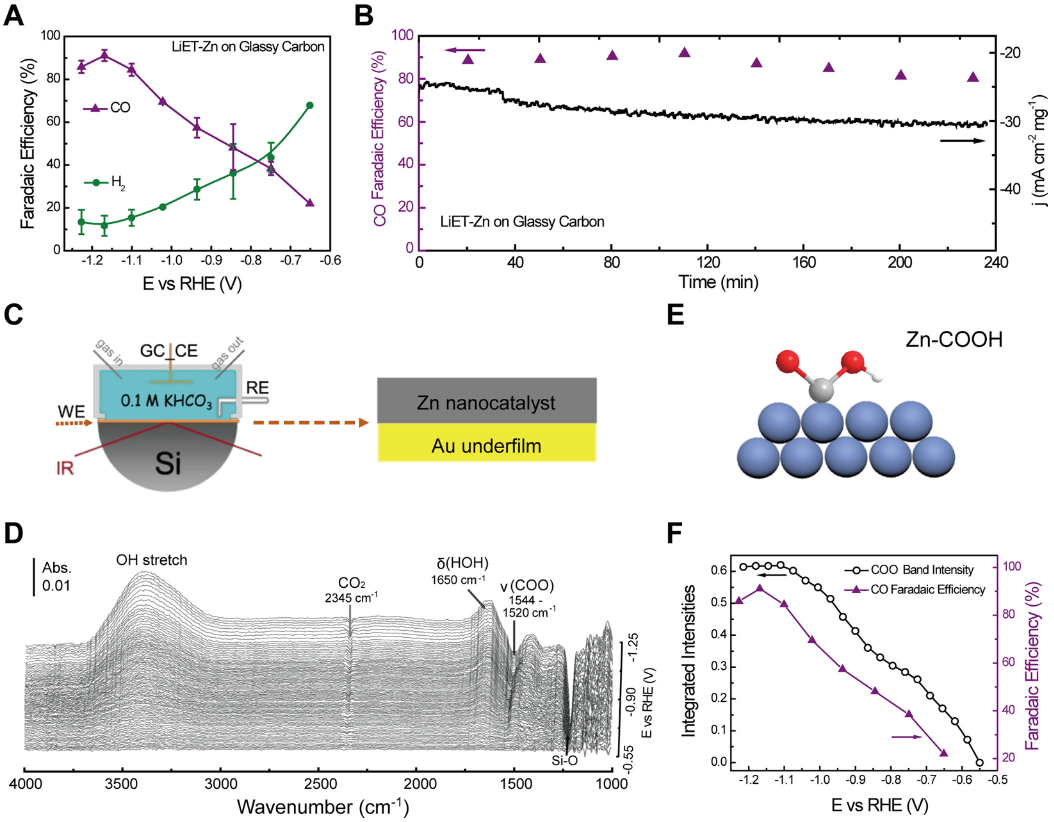

Figure 4. Electrocatalytic CO_2RR of LiET-Zn supported on glassy carbon electrode in CO_2-saturated 0.1 M $KHCO_3$. (A) FEs of H_2 and CO, and (B) long-term stability test at −1.17 V *vs* RHE of 0.2 mg cm^{-2} loading LiET-Zn. (C) Schematic illustration of ATR-SEIRAS cell employed in the present spectroelectrochemical measurements. (D) The *in situ* ATR-SEIRA spectra collected on a LiET-Zn cast Au/Si prism electrode with a time resolution of 2 s, using a single-beam spectrum at ∼ −0.55 V *vs* RHE in the same electrolyte as the reference spectrum. Each single-beam spectrum was an average of eight scans. (E) A schematic of the possible configuration of protonated *COOH intermediate adsorbed on Zn metal surface, Zn, C, O and H atoms are depicted as blue, gray, red, and white spheres. (F) Corresponding potential-dependent asymmetric stretch band intensities of ν_{as}(COO) at 1520−1544 cm^{-1} together with the CO FEs.

suppressed H_2 evolution (Figures 4A and S8), which is among the best reported CO_2RR performance on Zn-based catalysts (Table S1). Under a 4 h continuous electrolysis at −1.17 V *vs* RHE (Figure 4B), the overall current density gradually increases from 26.5 to 30 mA cm^{-2} mg^{-1} while maintaining a high CO FE of above 80%, demonstrating the good stability of the LiET-Zn catalysts.

Understanding the CO_2-to-CO reaction mechanisms is of great importance to the design of catalysts for further improved activities and selectivity, and our CO selective LiET-Zn can serve as a model catalyst for mechanism studies. In pursuit of a molecular-level understanding of the reaction pathway at the catalyst−electrolyte interface, advanced *in situ* ATR-SEIRAS[56] was employed to dynamically monitor the reactive intermediates evolution during potential sweep (Figures 4C and S9). Figure 4D shows the potentiodynamic SEIRA spectra measured in a CO_2-saturated 0.1 M $KHCO_3$ solution by applying linear sweeping voltammetry at 5 mV s^{-1} and a time resolution of 2 s. Two broad bands at 3200−3700 and 1650 cm^{-1} are assigned to ν(OH) and δ(HOH) of water.[57,58] No CO_{ad} band is found between 1800 and 2200 cm^{-1}, suggesting no appreciable underlying Au sites are exposed as well as a facile CO desorption from metallic Zn surface[59,60] (Figure S9). Since the spectra are defined in absorbance as $-\log(I/I_0)$, where I and I_0 represent the sample and reference single-beam spectra, therefore, the positive and negative bands herein account for the generated and the consumed species, respectively.[61] The negative-going peak at 2345 cm^{-1} arises from the depletion of dissolved CO_2 during negative potential sweep.[62,63] More interestingly, the asymmetric COO stretching vibration of adsorbed carboxyl species at ∼1520−1544 cm^{-1} is observed as downward peaks,[64−66] shedding some light on the possible reaction intermediates. This ν(COO) band frequency red-shifts (wavenumber decreasing) with a negative sweep potential, which is known as the Stark effect and indicates that the carboxyl species is bonded on a Zn surface,[67] with a possible adsorption configuration illustrated in Figure 4E. We further plot the ν(COO) band intensity in Figure 4F as a function of potential together with the corresponding CO FE. The positive correlation between carboxyl consumption and the CO selectivity strongly suggests the reaction intermediate of surface bonded carboxyl, which is gradually consumed and further reduced to CO under more negative potentials. In good agreement with Hori's electrochemical data and proposed mechanism on CO-evolution electrode,[23] the spectroelectrochemical results here clearly reveal that the surface-bonded carboxyl intermediate of $*COO^-$ contributes directly to the CO_2-to-CO conversion.

CONCLUSION

In summary, here we employed LIB technologies to create active GBs in ZnO and thus improve the activity and selectivity in CO_2-to-CO conversion. Given the wide variety of metal oxide materials studied in battery electrodes as well as the great importance of GBs in different electrocatalytic reactions especially in CO_2RR, we demonstrate a general approach of Li electrochemical tuning to improve the catalytic performances. In addition, the advanced *in situ* ATR-SEIRAS technique reveals the CO_2RR intermediates at molecular levels, providing mechanism understandings and thus important guidance for the design of next-generation catalysts.

METHODS

Materials Preparation. The ZnO NPs were directly synthesized on CFP electrode (AvCarb MGL270, FuelCellStore) by a previously developed dip-coating method. The solution of zinc nitrate was first prepared by dissolving 40 wt % $Zn(NO_3)_2 \cdot 6H_2O$ (Sigma-Aldrich) and 4 wt % PVP (M_w = 360,000, Sigma-Aldrich) into 56 wt % deionized water. Then 60 μL of the solution was pipetted onto O_2 plasma-treated CFP pieces (1 cm × 2 cm) and dried in vacuum. The $Zn(NO_3)_2$/CFP was then heated up to 350 °C in 1 h in air and kept there for another 1 h, where the $Zn(NO_3)_2$ was decomposed into ZnO NPs. The mass loading of Zn is measured to be ~3 mg cm^{-2}. The as-grown ZnO on CFP was made into a pouch cell battery with a piece of Li metal and a polymer separator (Celgard) soaked with organic electrolyte (1.0 M LiPF6 in 1:1 w/w ethylene carbonate/diethyl carbonate, BASF Chemicals) in a sandwich structure. No other binder or conductive carbon was needed. The galvanostatic cycling current was set at 0.3 mA cm^{-2} and cycled between 0.4 and 3 V *vs* Li^+/Li. The galvanostatic cycled Zn on CFP was then washed by deaerated isopropanol for further characterizations. The OD-Zn was prepared by electrochemically reducing ZnO/CFP in 0.1 M $KHCO_3$ aqueous solution at −0.63 V *vs* RHE for 30 min.

Commercial unsupported ZnO NPs (ReagentPlus grade, Sigma-Aldrich) were used as received for comparison. The Li tuning method is the same with LiET-Zn/CFP except using a piece of Al foil as the ZnO substrate in a pouch cell battery.

Materials Characterizations. The TEM characterization was carried out using a JEOL 2100 transmission electron microscope under 80 kV to avoid melting Zn NPs under high-energy electron beams. Powder X-ray diffraction data were collected using a Bruker D2 Phaser diffractometer in parallel beam geometry employing Cu Kα radiation and an one-dimensional LYNXEYE detector, at a scan speed of 0.02° per step and a holding time of 2 s per step. XPS was obtained with a Thermo Scientific K-Alpha ESCA spectrometer, using a monochromatic Al Kα radiation (1486.6 eV) and a low energy flood gun as neutralizer. The binding energy of C 1s peak at 284.6 eV was used as reference. Raman spectroscopy was carried out on a WITEC CRM200 confocal Raman spectrometer with a 532 nm laser source. Typically, a dispersion grating of 600 g mm^{-1} and a co-adding of 64 scans were applied in the spectral tests.

Electrochemical Measurements. All electrochemical measurements were run at 25 ± 1 °C in a customized gastight H-type glass cell separated by Nafion 117 membrane (Fuel Cell Store). A BioLogic VMP3 workstation was employed to record the electrochemical response. Certain amounts of $KHCO_3$ (99.95%, Sigma-Aldrich) was dissolved in Millipore water (18.2 MΩ·cm) to prepare the 0.1 M electrolyte, which was further purified by electrolysis between two graphite rods at 0.1 mA for 24 h to remove any trace amounts of metal ions.

In a typical three-electrodes test system, a platinum foil (99.99%, Beantown Chemical) and a saturated calomel electrode (SCE, CH Instruments) were used as the counter and reference electrodes, respectively. ZnO/CFP and LiET-Zn/CFP can be used directly as the working electrode. For commercial ZnO or LiET-Zn powder, typically 5 mg of the powder was mixed with 0.5 mL of isopropanol, 0.5 mL of water, and 10 μL of Nafion 117 solution (5%, Sigma-Aldrich) and sonicated for 20 min to get a homogeneous catalyst ink. 80 μL of the ink was pipetted onto a fresh polished glassy carbon electrode (HTW GmbH, 1 cm × 2 cm, 0.2 mg cm^{-2} mass loading), which was vacuum-dried prior to usage.

All potentials measured against SCE were converted to the RHE scale in this work using E (*vs* RHE) = E (*vs* SCE) + 0.244 V + 0.0591 × pH, where pH values of electrolytes were determined by an Orion 320 PerpHecT LogR Meter (Thermo Scientific). Solution resistance (R_u) was determined by potentiostatic electrochemical impedance spectroscopy (PEIS) at frequencies ranging from 0.1 Hz to 200 kHz and manually compensated as E (iR corrected *vs* RHE) = E (*vs* RHE) − $R_u \times I$ (amps of average current).

CO_2 Reduction Products Analysis. During electrolysis, CO_2 gas (99.995%, Airgas) was delivered into the cathodic compartment containing CO_2-saturated electrolyte at a rate of 20.0 standard cubic centimeters per minute (sccm, monitored by Alicat Scientific mass flow controller) and vented into a gas chromatograph (GC, Shimadzu GC-2014) equipped with a combination of molecular sieve 5A, Hayesep Q, Hayesep T, and Hayesep N columns. A thermal conductivity detector (TCD) was mainly used to quantify H_2 concentration, and a flame ionization detector (FID) with a methanizer was used to quantitative analysis CO content and/or any other alkane species. The detectors are calibrated by two different concentrations (H_2: 100 and 1042 ppm; CO: 100 and 496.7 ppm) of standard gases. The gas products were sampled after a continuous electrolysis of ~20 min under each potential. The partial current density for a given gas product was calculated:

$$j_i = x_i \times v \times \frac{n_i F p_0}{RT} \times (\text{electrode area})^{-1}$$

where x_i is the volume fraction of certain product determined by online GC referenced to calibration curves from two standard gas samples (Scott and Airgas), v is the flow rate of 20.0 sccm, n_i is the number of electrons involved, p_0 = 101.3 kPa, F is the Faradaic constant, and R is the gas constant. The corresponding FE at each potential is calculated by FE = j_i/i_{total} × 100%.

***In Situ* IR Measurement.** For electrochemical ATR-SEIRAS measurement, 30 μL of LiET-Zn ink solution was casted onto the central area (confined by an O-ring with Φ = 8 mm) of an Au film chemically deposited on the basal plane of a hemicylindrical Si prism. Then the spectral measurements were run on a Nicolet IS50 FTIR spectrometer equipped with a liquid nitrogen cooled MCT-A detector at a bottom-up incidence angle of *ca.* 65°. All spectra were collected at a resolution of 8 cm^{-1} with p-polarized IR radiation by using a built-in ZnSe polarizer and shown in the absorbance unit as $-\log(I/I_0)$, where I and I_0 represent the intensities of the reflected radiation of the sample and reference spectra, respectively. Time resolution in potential-evolved spectral set is 2 s, and each single-beam spectrum was an average of eight scans. A CHI 440C electrochemistry workstation (CH Instruments, Inc.) was used for potential control.

ASSOCIATED CONTENT

Supporting Information

The Supporting Information is available free of charge on the ACS Publications website at DOI: 10.1021/acsnano.7b03029.

Additional XPS, TEM, spectroscopic and electrochemical characterizations, comparison of CO evolution performances on reported Zn electrocatalysts (PDF)

AUTHOR INFORMATION

Corresponding Author

*E-mail: hwang@rowland.harvard.edu.

ORCID

Kun Jiang: 0000-0003-3148-5058
Wen-Bin Cai: 0000-0003-0500-4791
Haotian Wang: 0000-0002-3552-8978

Author Contributions

H.W. and K.J. conceived the idea of this project. H.W. and K.J. performed materials synthesis and characterizations. H.W. and K.J. designed and performed the catalysis measurements. H.W., K.J., Han W., and W.B.C. designed the *in situ* ATR-SEIRAS measurement. Han W. performed the *in situ* ATR-SEIRAS experiment. H.W. and K.J. wrote the manuscript with the inputs from Han W. and W.B.C. H.W. supervised the project.

Notes

The authors declare no competing financial interest.

ACKNOWLEDGMENTS

This work was supported by the Rowland Junior Fellows Program at Rowland Institute, Harvard University. H.W. and K.J. acknowledge the great support from the Friend group at Harvard University and appreciate the insightful discussion with S. Siahrostami at SUNCAT. W.B.C. acknowledges the support from 973 Program of MOST (2015CB932303) and NSFC (21473039 and 21273046). This work was performed in part at the Center for Nanoscale Systems (CNS), a member of the National Nanotechnology Infrastructure Network (NNIN), which is supported by the National Science Foundation under NSF award no. ECS-0335765. CNS is part of Harvard University.

REFERENCES

(1) Obama, B. The Irreversible Momentum of Clean Energy. *Science* **2017**, *355*, 126−129.

(2) Chu, S.; Cui, Y.; Liu, N. The Path towards Sustainable Energy. *Nat. Mater.* **2017**, *16*, 16−22.

(3) Cook, T. R.; Dogutan, D. K.; Reece, S. Y.; Surendranath, Y.; Teets, T. S.; Nocera, D. G. Solar Energy Supply and Storage for the Legacy and Nonlegacy Worlds. *Chem. Rev.* **2010**, *110*, 6474−6502.

(4) Meyer, T. J. Chemical Approaches to Artificial Photosynthesis. *Acc. Chem. Res.* **1989**, *22*, 163−170.

(5) Liu, C.; Colón, B. C.; Ziesack, M.; Silver, P. A.; Nocera, D. G. Water Splitting−biosynthetic System with CO_2 Reduction Efficiencies Exceeding Photosynthesis. *Science* **2016**, *352*, 1210−1213.

(6) Lewis, N. S.; Nocera, D. G. Powering the planet: Chemical Challenges in Solar Energy Utilization. *Proc. Natl. Acad. Sci. U. S. A.* **2006**, *103*, 15729−15735.

(7) Sakimoto, K. K.; Wong, A. B.; Yang, P. Self-photosensitization of Nonphotosynthetic Bacteria for Solar-to-chemical Production. *Science* **2016**, *351*, 74−77.

(8) Asadi, M.; Kim, K.; Liu, C.; Addepalli, A. V.; Abbasi, P.; Yasaei, P.; Phillips, P.; Behranginia, A.; Cerrato, J. M.; Haasch, R.; et al. Nanostructured Transition metal Dichalcogenide Electrocatalysts for CO_2 Reduction in Ionic Liquid. *Science* **2016**, *353*, 467−470.

(9) Li, C. W.; Ciston, J.; Kanan, M. W. Electroreduction of Carbon Monoxide to Liquid Fuel on Oxide-derived Nanocrystalline Copper. *Nature* **2014**, *508*, 504−507.

(10) Gao, S.; Lin, Y.; Jiao, X.; Sun, Y.; Luo, Q.; Zhang, W.; Li, D.; Yang, J.; Xie, Y. Partially Oxidized Atomic Cobalt Layers for Carbon Dioxide Electroreduction to Liquid Fuel. *Nature* **2016**, *529*, 68−71.

(11) Lin, S.; Diercks, C. S.; Zhang, Y.-B.; Kornienko, N.; Nichols, E. M.; Zhao, Y.; Paris, A. R.; Kim, D.; Yang, P.; Yaghi, O. M.; Chang, C. J. Covalent Organic Frameworks Comprising Cobalt Porphyrins for Catalytic CO_2 Reduction in Water. *Science* **2015**, *349*, 1208−1213.

(12) Liu, M.; Pang, Y.; Zhang, B.; De Luna, P.; Voznyy, O.; Xu, J.; Zheng, X.; Dinh, C. T.; Fan, F.; Cao, C.; de Arquer, F. P.; Safaei, T. S.; Mepham, A.; Klinkova, A.; Kumacheva, E.; Filleter, T.; Sinton, D.; Kelley, S. O.; Sargent, E. H. Enhanced Electrocatalytic CO_2 Reduction *via* Field-induced Reagent Concentration. *Nature* **2016**, *537*, 382−386.

(13) Hansen, H. A.; Varley, J. B.; Peterson, A. A.; Nørskov, J. K. Understanding Trends in the Electrocatalytic Activity of Metals and Enzymes for CO_2 Reduction to CO. J. *J. Phys. Chem. Lett.* **2013**, *4*, 388−392.

(14) Hinnemann, B.; Moses, P. G.; Bonde, J.; Jørgensen, K. P.; Nielsen, J. H.; Horch, S.; Chorkendorff, I.; Nørskov, J. K. Biomimetic Hydrogen Evolution: MoS_2 Nanoparticles as Catalyst for Hydrogen Evolution. *J. Am. Chem. Soc.* **2005**, *127*, 5308−5309.

(15) Wang, H.; Lu, Z.; Xu, S.; Kong, D.; Cha, J. J.; Zheng, G.; Hsu, P.-C.; Yan, K.; Bradshaw, D.; Prinz, F. B.; Cui, Y. Electrochemical Tuning of Vertically Aligned MoS_2 Nanofilms and Its Application in Improving Hydrogen Evolution Reaction. *Proc. Natl. Acad. Sci. U. S. A.* **2013**, *110*, 19701−19706.

(16) Wang, H.; Xu, S.; Tsai, C.; Li, Y.; Liu, C.; Zhao, J.; Liu, Y.; Yuan, H.; Abild-Pedersen, F.; Prinz, F. B.; et al. Direct and Continuous Strain Control of Catalysts with Tunable Battery Electrode Materials. *Science* **2016**, *354*, 1031−1036.

(17) Zhu, W. L.; Michalsky, R.; Metin, O.; Lv, H. F.; Guo, S. J.; Wright, C. J.; Sun, X. L.; Peterson, A. A.; Sun, S. H. Monodisperse Au Nanoparticles for Selective Electrocatalytic Reduction of CO_2 to CO. *J. Am. Chem. Soc.* **2013**, *135*, 16833−16836.

(18) Chen, Y. H.; Li, C. W.; Kanan, M. W. Aqueous CO_2 Reduction at Very Low Overpotential on Oxide-Derived Au Nanoparticles. *J. Am. Chem. Soc.* **2012**, *134*, 19969−19972.

(19) Schreier, M.; Curvat, L.; Giordano, F.; Steier, L.; Abate, A.; Zakeeruddin, S. M.; Luo, J.; Mayer, M. T.; Gratzel, M. Efficient Photosynthesis of Carbon Monoxide from CO_2 Using Perovskite Photovoltaics. *Nat. Commun.* **2015**, *6*, 7326.

(20) Rosen, B. A.; Salehi-Khojin, A.; Thorson, M. R.; Zhu, W.; Whipple, D. T.; Kenis, P. J. A.; Masel, R. I. Ionic Liquid-Mediated Selective Conversion of CO_2 to CO at Low Overpotentials. *Science* **2011**, *334*, 643−644.

(21) Lu, Q.; Rosen, J.; Zhou, Y.; Hutchings, G. S.; Kimmel, Y. C.; Chen, J. G.; Jiao, F. A Selective and Efficient Electrocatalyst for Carbon Dioxide Reduction. *Nat. Commun.* **2014**, *5*, 3242.

(22) Yoon, Y.; Hall, A. S.; Surendranath, Y. Tuning of Silver Catalyst Mesostructure Promotes Selective Carbon Dioxide Conversion into Fuels. *Angew. Chem., Int. Ed.* **2016**, *55*, 15282−15286.

(23) Hori, Y.; Wakebe, H.; Tsukamoto, T.; Koga, O. Electrocatalytic Process of CO Selectivity in Electrochemical Reduction of CO_2 at Metal Electrodes in Aqueous Media. *Electrochim. Acta* **1994**, *39*, 1833−1839.

(24) Kuhl, K. P.; Hatsukade, T.; Cave, E. R.; Abram, D. N.; Kibsgaard, J.; Jaramillo, T. F. Electrocatalytic Conversion of Carbon Dioxide to Methane and Methanol on Transition Metal Surfaces. *J. Am. Chem. Soc.* **2014**, *136*, 14107−14113.

(25) Li, C. W.; Kanan, M. W. CO_2 Reduction at Low Overpotential on Cu Electrodes Resulting from the Reduction of Thick Cu_2O Films. *J. Am. Chem. Soc.* **2012**, *134*, 7231−7234.

(26) Verdaguer-Casadevall, A.; Li, C. W.; Johansson, T. P.; Scott, S. B.; McKeown, J. T.; Kumar, M.; Stephens, I. E. L.; Kanan, M. W.; Chorkendorff, I. Probing the Active Surface Sites for CO Reduction on Oxide-Derived Copper Electrocatalysts. *J. Am. Chem. Soc.* **2015**, *137*, 9808−9811.

(27) Eilert, A.; Cavalca, F.; Roberts, F. S.; Osterwalder, J.; Liu, C.; Favaro, M.; Crumlin, E. J.; Ogasawara, H.; Friebel, D.; Pettersson, L. G. M.; Nilsson, A. Subsurface Oxygen in Oxide-Derived Copper Electrocatalysts for Carbon Dioxide Reduction. *J. Phys. Chem. Lett.* **2017**, *8*, 285−290.

(28) Ren, D.; Deng, Y.; Handoko, A. D.; Chen, C. S.; Malkhandi, S.; Yeo, B. S. Selective Electrochemical Reduction of Carbon Dioxide to Ethylene and Ethanol on Copper (I) Oxide Catalysts. *ACS Catal.* **2015**, *5*, 2814−2821.

(29) Ma, M.; Djanashvili, K.; Smith, W. A. Controllable Hydrocarbon Formation from the Electrochemical Reduction of CO_2 over Cu Nanowire Arrays. *Angew. Chem.* **2016**, *128*, 6792−6796.

(30) Roberts, F. S.; Kuhl, K. P.; Nilsson, A. Electroreduction of Carbon Monoxide Over a Copper Nanocube Catalyst: Surface Structure and pH Dependence on Selectivity. *ChemCatChem* **2016**, *8*, 1119−1124.

(31) Alves, D. C. B.; Silva, R.; Voiry, D.; Asefa, T.; Chhowalla, M. Copper Nanoparticles Stabilized by Reduced Graphene Oxide for CO_2 Reduction Reaction. *Mater. Renew. Sustain. Energy* **2015**, *4*, 2.

(32) Gao, S.; Jiao, X. C.; Sun, Z. T.; Zhang, W. H.; Sun, Y. F.; Wang, C. M.; Hu, Q. T.; Zu, X. L.; Yang, F.; Yang, S. Y.; Liang, L.; Wu, J.; Xie, Y. Ultrathin Co_3O_4 Layers Realizing Optimized CO_2 Electroreduction to Formate. *Angew. Chem., Int. Ed.* **2016**, *55*, 698−702.

(33) Chen, Y. H.; Kanan, M. W. Tin Oxide Dependence of the CO_2 Reduction Efficiency on Tin Electrodes and Enhanced Activity for

DOI: 10.1021/acsnano.7b03029
ACS Nano XXXX, XXX, XXX−XXX

Tin/Tin Oxide Thin-Film Catalysts. *J. Am. Chem. Soc.* **2012**, *134*, 1986−1989.

(34) Zhang, S.; Kang, P.; Meyer, T. J. Nanostructured Tin Catalysts for Selective Electrochemical Reduction of Carbon Dioxide to Formate. *J. Am. Chem. Soc.* **2014**, *136*, 1734−1737.

(35) Dutta, A.; Kuzume, A.; Rahaman, M.; Vesztergom, S.; Broekmann, P. Monitoring the Chemical State of Catalysts for CO_2 Electroreduction: An In Operando Study. *ACS Catal.* **2015**, *5*, 7498−7502.

(36) Lei, F.; Liu, W.; Sun, Y.; Xu, J.; Liu, K.; Liang, L.; Yao, T.; Pan, B.; Wei, S.; Xie, Y. Metallic Tin Quantum Sheets Confined in Graphene toward High-efficiency Carbon Dioxide Electroreduction. *Nat. Commun.* **2016**, *7*, 12697.

(37) Rosen, J.; Hutchings, G. S.; Lu, Q.; Forest, R. V.; Moore, A.; Jiao, F. Electrodeposited Zn Dendrites with Enhanced CO Selectivity for Electrocatalytic CO_2 Reduction. *ACS Catal.* **2015**, *5*, 4586−4591.

(38) Quan, F. J.; Zhong, D.; Song, H. C.; Jia, F. L.; Zhang, L. Z. A Highly Efficient Zinc Catalyst for Selective Electroreduction of Carbon Dioxide in Aqueous NaCl Solution. *J. Mater. Chem. A* **2015**, *3*, 16409−16413.

(39) Jiang, X. L.; Cai, F.; Gao, D. F.; Dong, J. H.; Miao, S.; Wang, G. X.; Bao, X. H. Electrocatalytic Reduction of Carbon Dioxide over Reduced Nanoporous Zinc Oxide. *Electrochem. Commun.* **2016**, *68*, 67−70.

(40) Won, D. H.; Shin, H.; Koh, J.; Chung, J.; Lee, H. S.; Kim, H.; Woo, S. I. Highly Efficient, Selective, and Stable CO_2 Electroreduction on a Hexagonal Zn Catalyst. *Angew. Chem., Int. Ed.* **2016**, *55*, 9297−9300.

(41) Yano, H.; Tanaka, T.; Nakayama, M.; Ogura, K. Selective Electrochemical Reduction of CO_2 to Ethylene at a Three-phase Interface on Copper (I) Halide-confined Cu-mesh Electrodes in Acidic Solutions of Potassium Halides. *J. Electroanal. Chem.* **2004**, *565*, 287−293.

(42) Cao, Z.; Kim, D.; Hong, D.; Yu, Y.; Xu, J.; Lin, S.; Wen, X.; Nichols, E. M.; Jeong, K.; Reimer, J. A.; et al. A Molecular Surface Functionalization Approach to Tuning Nanoparticle Electrocatalysts for Carbon Dioxide Reduction. *J. Am. Chem. Soc.* **2016**, *138*, 8120−8125.

(43) Ma, S.; Sadakiyo, M.; Heima, M.; Luo, R.; Haasch, R. T.; Gold, J. I.; Yamauchi, M.; Kenis, P. J. A. Electroreduction of Carbon Dioxide to Hydrocarbons Using Bimetallic Cu−Pd Catalysts with Different Mixing Patterns. *J. Am. Chem. Soc.* **2017**, *139*, 47−50.

(44) Li, Q.; Fu, J.; Zhu, W.; Chen, Z.; Shen, B.; Wu, L.; Xi, Z.; Wang, T.; Lu, G.; Zhu, J. J.; Sun, S. Tuning Sn-Catalysis for Electrochemical Reduction of CO_2 to CO *via* the Core/Shell Cu/SnO_2 Structure. *J. Am. Chem. Soc.* **2017**, *139*, 4290−4293.

(45) Kim, D.; Resasco, J.; Yu, Y.; Asiri, A. M.; Yang, P. Synergistic Geometric and Electronic Effects for Electrochemical Reduction of Carbon Dioxide Using Gold-copper Bimetallic Nanoparticles. *Nat. Commun.* **2014**, *5*, 4948.

(46) Kornienko, N.; Zhao, Y.; Kley, C. S.; Zhu, C.; Kim, D.; Lin, S.; Chang, C. J.; Yaghi, O. M.; Yang, P. Metal−organic Frameworks for Electrocatalytic Reduction of Carbon Dioxide. *J. Am. Chem. Soc.* **2015**, *137*, 14129−14135.

(47) Zhang, X.; Wu, Z.; Zhang, X.; Li, L.; Li, Y.; Xu, H.; Li, X.; Yu, X.; Zhang, Z.; Liang, Y.; Wang, H. Highly Selective and Active CO_2 Reduction Electrocatalysts Based on Cobalt Phthalocyanine/carbon Nanotube Hybrid Structures. *Nat. Commun.* **2017**, *8*, 14675.

(48) Weng, Z.; Jiang, J.; Wu, Y.; Wu, Z.; Guo, X.; Materna, K. L.; Liu, W.; Batista, V. S.; Brudvig, G. W.; Wang, H. Electrochemical CO_2 Reduction to Hydrocarbons on a Heterogeneous Molecular Cu Catalyst in Aqueous Solution. *J. Am. Chem. Soc.* **2016**, *138*, 8076−8079.

(49) Ma, M.; Trzesniewski, B. J.; Xie, J.; Smith, W. A. Selective and Efficient Reduction of Carbon Dioxide to Carbon Monoxide on Oxide-Derived Nanostructured Silver Electrocatalysts. *Angew. Chem., Int. Ed.* **2016**, *55*, 9748−9752.

(50) Kamada, K.; Enomoto, N.; Hojo, J. Metal Plating *via* Electrochemical Reduction of Oxide Layers Formed by Electrophoretic Deposition. *J. Ceram. Soc. Jpn.* **2009**, *117*, 926−928.

(51) Voiry, D.; Yamaguchi, H.; Li, J.; Silva, R.; Alves, D. C. B.; Fujita, T.; Chen, M.; Asefa, T.; Shenoy, V. B.; Eda, G.; Chhowalla, M. Enhanced Catalytic Activity in Strained Chemically Exfoliated WS_2 Nanosheets for Hydrogen Evolution. *Nat. Mater.* **2013**, *12*, 850−855.

(52) Poizot, P.; Laruelle, S.; Grugeon, S.; Dupont, L.; Tarascon, J. Nano-sized Transition-metal Oxides as Negative-electrode Materials for Lithium-ion Batteries. *Nature* **2000**, *407*, 496−499.

(53) Wang, H.; Lee, H. W.; Deng, Y.; Lu, Z.; Hsu, P. C.; Liu, Y.; Lin, D.; Cui, Y. Bifunctional Non-noble Metal Oxide Nanoparticle Electrocatalysts through Lithium-induced Conversion for Overall Water Splitting. *Nat. Commun.* **2015**, *6*, 7261.

(54) Srikant, V.; Clarke, D. R. On the Optical Band Gap of Zinc Oxide. *J. Appl. Phys.* **1998**, *83*, 5447−5451.

(55) Kärber, E.; Raadik, T.; Dedova, T.; Krustok, J.; Mere, A.; Mikli, V.; Krunks, M. Photoluminescence of Spray Pyrolysis Deposited ZnO Nanorods. *Nanoscale Res. Lett.* **2011**, *6*, 359.

(56) Osawa, M. Dynamic Processes in Electrochemical Reactions Studied by Surface-enhanced Infrared Absorption Spectroscopy (SEIRAS). *Bull. Chem. Soc. Jpn.* **1997**, *70*, 2861−2880.

(57) Baruch, M. F.; Pander, J. E.; White, J. L.; Bocarsly, A. B. Mechanistic Insights into the Reduction of CO_2 on Tin Electrodes Using *in situ* ATR-IR Spectroscopy. *ACS Catal.* **2015**, *5*, 3148−3156.

(58) Wuttig, A.; Liu, C.; Peng, Q.; Yaguchi, M.; Hendon, C. H.; Motobayashi, K.; Ye, S.; Osawa, M.; Surendranath, Y. Tracking a Common Surface-Bound Intermediate during CO_2-to-Fuels Catalysis. *ACS Cent. Sci.* **2016**, *2*, 522−528.

(59) Wang, Y.; Woll, C. IR Spectroscopic Investigations of Chemical and Photochemical Reactions on Metal Oxides: Bridging the Materials Gap. *Chem. Soc. Rev.* **2017**, *46*, 1875−1932.

(60) Scarano, D.; Bertarione, S.; Spoto, G.; Zecchina, A.; Otero Areán, C. FTIR Spectroscopy of Hydrogen, Carbon Monoxide, and Methane Adsorbed and Co-adsorbed on Zinc Oxide. *Thin Solid Films* **2001**, *400*, 50−55.

(61) Wang, H.; Jiang, B.; Zhao, T.-T.; Jiang, K.; Yang, Y.-Y.; Zhang, J.; Xie, Z.; Cai, W.-B. Electrocatalysis of Ethylene Glycol Oxidation on Bare and Bi-Modified Pd Concave Nanocubes in Alkaline Solution: An Interfacial Infrared Spectroscopic Investigation. *ACS Catal.* **2017**, *7*, 2033−2041.

(62) Jiang, K.; Xu, K.; Zou, S.; Cai, W.-B. B-Doped Pd Catalyst: Boosting Room-temperature Hydrogen Production from Formic Acid−Formate Solutions. *J. Am. Chem. Soc.* **2014**, *136*, 4861−4864.

(63) Gao, D.; Zhou, H.; Cai, F.; Wang, D.; Hu, Y.; Jiang, B.; Cai, W.-B.; Chen, X.; Si, R.; Yang, F.; Miao, S.; Wang, J.; Wang, G.; Bao, X. Switchable CO_2 Electroreduction *via* Engineering Active Phases of Pd Nanoparticles. *Nano Res.* **2017**, *10*, 2181−2191.

(64) Firet, N. J.; Smith, W. A. Probing the Reaction Mechanism of CO_2 Electroreduction over Ag Films *via* Operando Infrared Spectroscopy. *ACS Catal.* **2017**, *7*, 606−612.

(65) Zeleňák, V.; Vargová, Z.; Györyová, K. Correlation of Infrared Spectra of Zinc(II) Carboxylates with Their Structures. *Spectrochim. Acta, Part A* **2007**, *66*, 262−272.

(66) Noei, H.; Wöll, C.; Muhler, M.; Wang, Y. Activation of Carbon Dioxide on ZnO Nanoparticles Studied by Vibrational Spectroscopy. *J. Phys. Chem. C* **2011**, *115*, 908−914.

(67) Dunwell, M.; Lu, Q.; Heyes, J. M.; Rosen, J.; Chen, J. G.; Yan, Y.; Jiao, F.; Xu, B. The Central Role of Bicarbonate in the Electrochemical Reduction of Carbon Dioxide on Gold. *J. Am. Chem. Soc.* **2017**, *139*, 3774−3783.